Semi-automated design strategy for multi-stable magnetic out-of-plane actuators with accurate pre-defined positions

Pascal M. Weber, Michael Olbrich, Yannik T. Rüde, Christoph Ament, Ulrike Wallrabe

Angaben zur Veröffentlichung / Publication details:

Weber, Pascal M., Michael Olbrich, Yannik T. Rüde, Christoph Ament, and Ulrike Wallrabe. 2026. "Semi-automated design strategy for multi-stable magnetic out-of-plane actuators with accurate pre-defined positions." *Sensors and Actuators A: Physical* 410 (part 2): 118309. https://doi.org/10.1016/j.sna.2026.118309.

Sensors & Actuators: A. Physical 410 (2026) 118309

Contents lists available at ScienceDirect

Sensors and Actuators: A. Physical

journal homepage: www.journals.elsevier.com/sensors-and-actuators-a-physical

Semi-automated design strategy for multi-stable magnetic out-of-plane actuators with accurate pre-defined positions

Pascal M. Weber [a,1,*], Michael Olbrich [b,1], Yannik T. Rüde [a], Christoph Ament [b], Ulrike Wallrabe [a]

[a] Laboratory for Microactuators, Department of Microsystems Engineering (IMTEK), University of Freiburg, Georges-Köhler-Allee 102, Freiburg, 79110, BW, Germany
[b] Chair of Control Engineering, Faculty of Applied Computer Science, University of Augsburg, Am Technologiezentrum 8, Augsburg, 86159, BY, Germany

HIGHLIGHTS

- Multi-stable magnetic actuator design realized, by permanent magnet and mu-metal rings.
- Accurate, fast-to-evaluate phenomenological magnetic force model for single rings.
- Superposition of single forces accurately describes multi-ring configurations.
- Robust configurations with desired equilibrium locations achieved by automated design.

ARTICLE INFO

Keywords:
Model-based optimization
Large vertical displacement
Magnetic actuator
Multi-stability
Reluctance force
Requirements-driven design

ABSTRACT

This work presents an analytical modeling approach for the semi-automated design of magnetic actuators with multiple pre-defined stable positions. The analyzed system allows for large out-of-plane displacements of a freely movable permanent magnetic plunger that is actuated by electromagnetic coils for switching between multiple stable resting positions, in which the plunger can be held without the need for further continuous energy consumption. These equilibrium positions are generated by the reluctance force between several mu-metal rings and the permanent magnet. Instead of computationally expensive finite element modeling, a phenomenological model is derived that describes the force contribution of single mu-metal rings depending on their dimensions. We exploit this analytical computation to accurately describe arbitrary multi-ring configurations, enabling an efficient analysis and design procedure. This model then provides the foundation for a requirements-driven design approach, in which pre-defined stable positions are used to derive the corresponding mu-metal ring configuration. In this context, the robustness of the system in terms of force barriers between the stable states is also considered. This eventually enables an automated design process that significantly reduces the complexity compared to manually designing application-specific setups. The modeling and design approaches are validated experimentally, showing good agreement between the predicted and measured force-displacement curves.

1. Introduction

Optimizing design parameters is an important step in the development of every actuator. Particularly for multi-stable systems, properties such as the locations of equilibrium positions and the energy barriers between them may need to be tuned for a specific application. Such actuators can generally be categorized into systems whose stable resting positions are physically enforced by mechanical contacts, systems that are intrinsically multi-stable due to nonlinear physical effects that generate an energy landscape, and actuators that combine both principles.

The first category includes actuators that rely on mechanical stoppers [1], which are typically used to achieve bistability and, in some cases, quadstability [2]. An alternative concept that can generally realize an arbitrary number of stable resting positions is the use of toothed holding arms that lock into corresponding racks on the mobile part [3,4].

Intrinsic multi-stability, by contrast, is often achieved through nonlinear structural effects. A common type is the bistable buckling beam

* Corresponding author.
Email address: pascal.weber@imtek.uni-freiburg.de (P.M. Weber).

[1] The authors contributed equally to this work.

https://doi.org/10.1016/j.sna.2026.118309
Received 16 April 2026; Received in revised form 7 July 2026; Accepted 22 July 2026
Available online 29 July 2026

[5,6], which can be extended to multi-stable behavior by combining several such elements [7].

In these systems, the nonlinear energy landscape results from restoring forces due to the spring-like behavior of the beams, resulting in positive stiffness around stable equilibria and negative stiffness in between. A similar effect occurs in buckled membranes, which are particularly useful in applications such as microvalves [8].

Many actuator designs combine these principles by using both mechanical stoppers and restoring-force-based equilibria. In such cases, a floating position may either replace one of the contact points [9,10] or extend the actuator by an additional equilibrium between mechanical stoppers [11].

Despite these diverse design approaches, most studies on multi-stable systems primarily focus on achieving multiple resting positions and maximizing stroke, rather than precisely tuning equilibrium locations or the energy barriers between them.

Only a few works explicitly address such design objectives. For example, Hussein et al. [12] present a buckling beam with electrothermal loading that enables post-fabrication tuning of stable positions by adjusting the beam stiffness. In contrast, Schomburg and Goll [13] derive an optimality criterion for maximizing the difference between inlet and actuation pressure in the microvalve presented in [8], which is closely related to the combined optimization of force barriers and required input energy.

Particularly for intrinsically multi-stable systems, determining the exact positions of more than two equilibria is already a challenging task that quickly becomes infeasible to do manually when combined with additional requirements on the energy barrier, i.e., robustness. This is because both the resting positions and the robustness are generally nonlinearly coupled and depend on multiple system parameters, preventing the independent optimization of these design objectives.

In particular, the combined adaptation of force barriers and the precise locations of resting positions is a complex problem that, to the best of our knowledge, has not yet been addressed in the literature.

To address this challenge, we present a model-based optimization approach that can be applied to achieve such a requirements-driven design. We demonstrate its effectiveness on the magnetically actuated lift actuator introduced in [14], which has multiple stable positions for a permanent magnetic plunger. These positions, as well as the corresponding force barriers between them, are defined by the reluctance forces of several mu-metal rings and are therefore determined by the locations and dimensions of those rings. However, the adjustment of these parameters is nontrivial, as each magnetic ring influences multiple neighboring stable states, further emphasizing the need for a systematic design approach.

When designing systems according to specific requirements, model-based optimization is commonly applied to tune the variable design parameters. Particularly in the field of microsystems, the static and dynamic behavior often depends on nonlinear partial differential equations, for example due to electrostatic, magnetic, or elastic effects. In such cases, analytical solutions often only exist for simple configurations or are approximated for small displacements as the movable part is typically suspended by cantilevers. Therefore, finite element (FE) methods are typically applied and have been successfully implemented within numerical optimization algorithms [15,16]. However, FE analysis is computationally expensive and a large number of model evaluations are typically required for nonlinear optimization problems. The incorporation of FE models can therefore easily become impractical.

To reduce the computational effort, surrogate models [17] or analytical approximations [18,19] are a viable alternatives in many cases. While this allows for an analytical solution in individual cases [20], numerical optimization algorithms are generally used. A popular solver choice is the genetic algorithm [18,19,21], which is practical for nonlinear problems due to its global behavior and the fact that a sufficiently accurate initial guess for the optimization parameters is not required.

In the following, we apply numerical optimization to the multi-stable magnetic lift actuator to determine suitable dimensions and locations of the mu-metal rings in accordance with user-defined specifications (e.g., resting positions and the force barrier between them). A genetic algorithm is used since it allows the incorporation of integer-valued variables, which is necessary when only a discrete set of predefined mu-metal rings and spacers in between these rings can be used. While in general, models used for design optimizations are often physically motivated and verified by FE models, these are typically only available for special cases of magnetic systems. Moreover, as shown in [22], such FE models may require additional material parameter calibration based on experimental data to ensure accurate behavior. Instead, we propose an approximation directly based on experimental data, i.e., a phenomenological model.

2. Design of the multi-stable lift actuator

Starting point for the optimization is our actuator design, which is similar to the one presented in [14]. A sectional view of this actuator is shown in Fig. 1.

The movable plunger in the center can slide freely up and down within the linear bearing without any physical connection to the rest of the actuator. The linear bearing has an inner diameter of 2.2mm and a wall thickness of only 250μm. The actuation mechanism consists of four identical fixed coils and a neodymium permanent magnet (N40) within the plunger. The plunger has a total mass of 0.12 g and is made of the magnet, measuring 1mm in height, 2mm in diameter, positioned between two polyoxymethylene (POM) rods. These rods improve guidance and lateral stability while also enabling the attachment of a potential payload to the magnet.

To pull the magnet into one of the actuation coils, a short positive current pulse is applied to the coil. This behavior is shown in Fig. 2, where current pulses of 500 mA and 20 ms duration are used to move the plunger between stable positions. Because of the relative orientation of the magnet and the coil, the magnet is pulled into the coil, regardless of whether it is positioned above or below it. Similarly, it could be pushed away with a negative current trajectory. As shown in Fig. 2(a), each transition is followed by an overshoot of up to 866 μm, followed by damped oscillations at approximately 18.4 Hz.

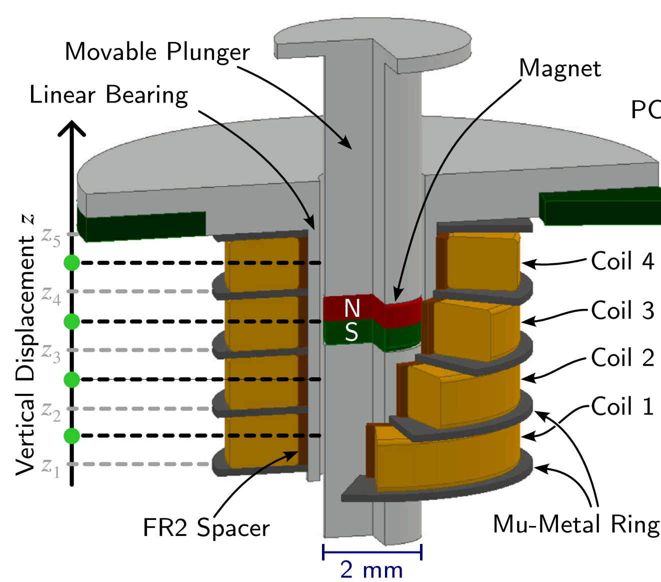

Fig. 1. Cross-section of the actuator [14], with the plunger sliding freely up and down within the linear bearing. The mu-metal rings are mounted in their positions z_i using FR2 spacers. The space between the mu-metal rings is used to wind four actuation coils around the linear bearing.

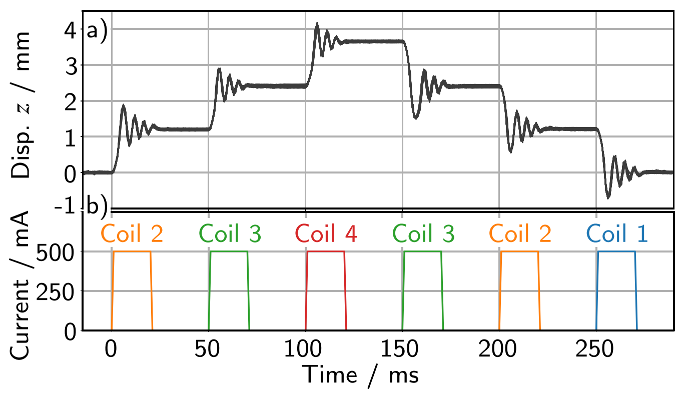

Fig. 2. Dynamic actuation of the plunger, starting from the stable position associated with coil 1. Measured plunger position during 100 repeated actuation cycles a), illustrating the repeatability of the motion. Corresponding current trajectories of the actuation coils b), color-coded by coil. (For interpretation of the references to colour in this figure legend, the reader is referred to the web version of this article.)

The figure shows the results of one hundred repeated measurements, demonstrating a high degree of repeatability. The maximum deviation between measurements within a stable position remains below 100 μm.

Once the magnet reaches a certain position within the actuated coil (green markers in Fig. 1), it can be held in place indefinitely without any further energy consumption, as is demonstrated by the actuation currents shown in Fig. 2(b). These stable positions are created by placing five mu-metal rings around the linear bearing, which hold the magnet in place via the reluctance force. The mu-metal rings have an outer diameter of up to 6.5 mm and a thickness of 100 μm. They are laser cut from *MagnoShield FLEX* sheet material [23] using a UV laser (*Trumpf TruMark*). The spacing between the mu-metal rings is defined by narrow spacer rings cut from phenolic paper (FR2) sheets that are combined from two available thicknesses (0.32 mm and 0.5 mm) to match the desired spacing.

Most importantly, the design is readily adaptable. Additional coils and mu-metal rings can provide more stable positions, while adjustments to the ring geometry and placement allow tuning of the reluctance force, the latter of which we provide a guide for in this paper.

3. Characterization of single mu-metal rings

We will first characterize the position-dependent reluctance force of a single mu-metal ring by means of an analytical approximation. This mathematical formulation can later be used to approximate the overall force with multiple mu-metal rings. For this purpose, we constructed a simple test jig, similar in design to the actuator, that can hold a single mu-metal ring of varying sizes. To measure the force–displacement behavior, the plunger was connected to a vertical stage via a force sensor (*KD34s*) and incrementally pulled through the linear guide while measuring the force at each step. A visualization is presented in Fig. 3(a), however, rotated by 90° compared to Fig. 1. The two stable positions above and below the ring are indicated. Fig. 3(b) plots the magnetic reluctance force for varying inner diameters and a fixed outer diameter of 6.5 mm.

To utilize point symmetry, we define the zero displacement as the position where the magnet is centered within the mu-metal ring. Fig. 3(b) clearly displays the two stable positions, where a downward movement results in an upward force, and vice versa. These stable positions are symmetrically located at approximately ± 0.8mm.

To describe this behavior, several approaches have been considered. In [24], a Boundary Element Method (BEM) was presented that can be adapted to calculate the force between a permanent magnet and a soft magnetic ring.

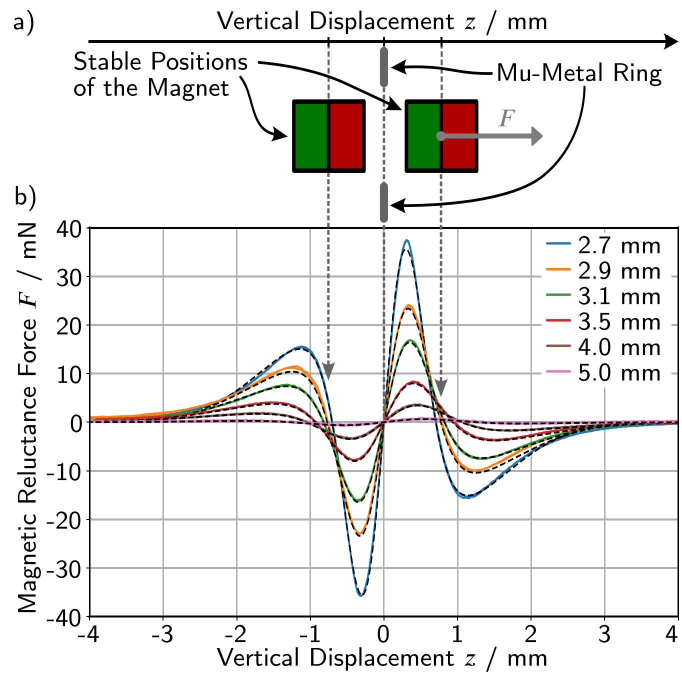

Fig. 3. a) Illustration of the two stable positions of the magnet on either side of the mu-metal ring. b) Force-displacement measurements between the magnet and a single mu-metal ring with an outer diameter d_{out} = 6.5 mm and varying inner diameters d_{in}. The black dashed lines represent fits using the function defined in Eq. (1). (For interpretation of the references to colour in this figure legend, the reader is referred to the web version of this article.)

This approach was less computationally expensive than a traditional FE analysis and the resulting solution could reproduce the general shape of the measured behavior well. However, it was quantitatively too imprecise, which renders this approach unsuitable for our optimization.

As a heuristic approximation, the mu-metal ring could also be modeled as a permanent magnetic ring to investigate whether this simplified representation allows the force-displacement behavior to be calculated. In [25], an approach to calculate the magnetic field of axially symmetric permanent magnets by piecewise approximations was derived. This method was also applied to ring magnets, where the magnetic field was calculated by negative superposition. In other words, we can calculate the magnetic field of a cylindrical magnet whose outside diameter matches that of the ring magnet, and then subtract the magnetic field of a second cylindrical magnet representing the hole in the ring with the same magnetization.

Based on the gradient of the resulting magnetic field, the force exerted on another magnet can be determined using volume integrals. For ring magnets, the negative superposition of the magnetic field also applies to the force, due to the linearity of integrals. This allows for the direct application of established models for the force calculations between cylindrical permanent magnets, rather than solving volume integrals based on an approximated magnetic field.

A suitable closed-form solution was presented by Robertson [26], in which the force between two cylindrical magnets is computed semi-analytically using elliptic integrals. Using the negative superposition previously mentioned in [25], this can be modified to a configuration with ring magnets. With suitable initial parameters, the resulting function can be fitted to the measurement data, as shown in Fig. 4(a). For comparison, we also plotted the prediction obtained by BEM [24], FEM (Ansys) and their deviations from the measurement in Fig. 4(b).

Because of the simplified assumption that the mu-metal ring can be represented as a permanent magnet, the twelve fitted parameters of the Robertson model deviate substantially from the actual physical parameters of the system.

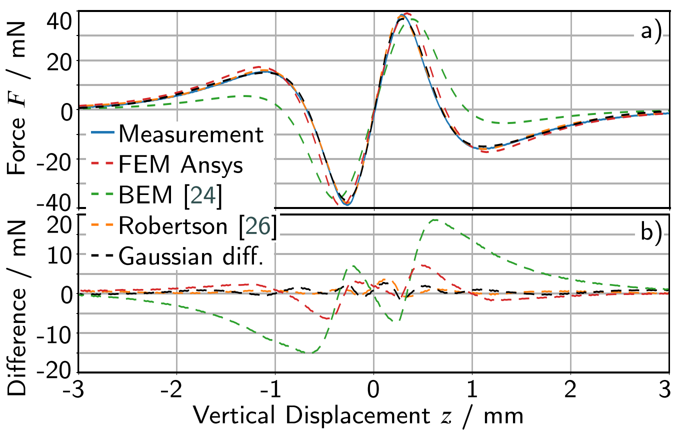

Fig. 4. a) Force displacement measurement (blue) alongside the predictions computed via Finite Element Method (FEM) (red), Boundary Element Method (BEM) [24] (green), Robertson [26] (orange), and our proposed Gaussian Eq. (1) (black). b) Shows the difference between these predictions and the real measurement. (For interpretation of the references to colour in this figure legend, the reader is referred to the web version of this article.)

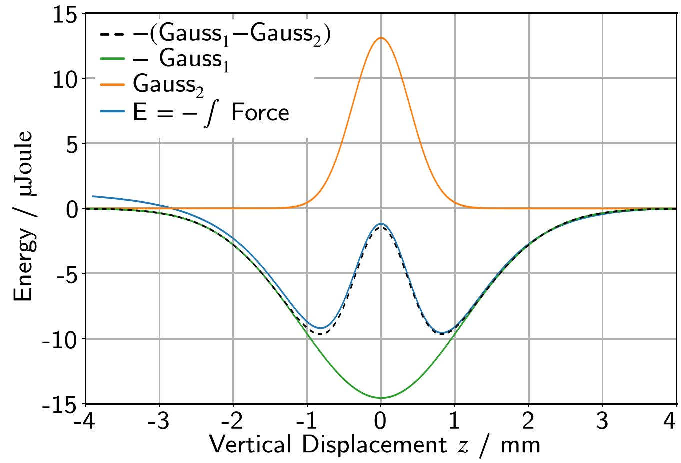

Fig. 5. Energy of the system (blue), obtained by integrating the measured force for a mu-metal ring with an inner diameter of 3.1 mm and an outer diameter of 6.5 mm. The black dashed line represents the subtraction of two Gaussian functions, calculated using the parameters fitted in Fig. 3. The individual Gaussian components are shown in green and orange. (For interpretation of the references to colour in this figure legend, the reader is referred to the web version of this article.)

As a result, the fitted model parameters cannot be directly related to design variables such as the inner and outer diameters of the mu-metal rings. Consequently, a separate characterization study would still be required to determine the Robertson parameters for each mu-metal ring. Since these parameters have no clear physical interpretation in the present application, this approach offers little advantage over the direct utilization of the measurements after denoising by function approximation.

Besides the accuracy of the prediction, the required time to evaluate the force-displacement characteristic is a critical factor for an automated design. To calculate the characteristic within the range of ±4 mm with a resolution of 32pt/mm as used later, an average time of 5.84 s was necessary for BEM [24] of Vučković, while the method according to Robertson [26] required 20.98 s. While these times are very short compared to FEM (17min), they are nevertheless significantly too high to be used in our proposed optimization approach that requires an average of 4.7×10^5 function evaluations due to the high complexity of the problem. With current state-of-the-art methods, the fastest method to evaluate arbitrary mu-metal rings would be to interpolate between a grid of force-displacement curves which have been pre-calculated using FEM. We found that such an interpolation with 32 grid points requires 0.608 s. Given the high number of function evaluations, however, we are aiming for a model that can be computed in the range of milliseconds.

With regard to the lack of a faster-to-calculate analytical solution in literature, we propose the use of two weighted derivatives of Gaussian bell curves subtracted from one another, as given in (1).

$$
\begin{aligned}
F(z) =& \overbrace{w_1 \frac{z}{\sigma_1^3 \sqrt{2\pi}} \exp\left(-\frac{1}{2}\left(\frac{z}{\sigma_1}\right)^2\right)}^{\text{Derivative of Gaussian}_1} \\
& \underbrace{-w_2 \frac{z}{\sigma_2^3 \sqrt{2\pi}} \exp\left(-\frac{1}{2}\left(\frac{z}{\sigma_2}\right)^2\right)}_{\text{Derivative of Gaussian}_2}
\end{aligned}
\tag{1}
$$

Here, w_1, w_2 correspond to weighting factors, and σ_1, σ_2 to the Gaussian widths. Compared with the previous methods, this approach can be computed in a reasonable time, requiring an average of only 0.34 ms. While maintaining a maximum deviation of less than 3 mN (Fig. 4b), comparable to Robertson [26], it allows us to easily describe the force–displacement behavior of different mu-metal rings, as shown in Fig. 3(b) (dashed black line). This makes it the method of choice for our further analysis.

The selection of this function was not arbitrary but was motivated by an examination of the system's energy, obtained by integrating the measured force, as shown in Fig. 5 (blue). The characteristic shape of this energy directly suggested the use of a Gaussian-type approximation for describing the system's behavior.

The dashed black line in Fig. 5 represents the subtraction of two weighted Gaussian curves (without derivatives), generated using the parameters obtained from the force fit in Fig. 3. For clarity, the two individual weighted Gaussian curves are also plotted in green and orange. The subtraction provides an accurate representation of the energy derived from the force measurements, despite a slight drift in the energy caused by the integration process, which accumulates small measurement errors. The two stable positions discussed previously are clearly visible here as the minima in the energy plot.

To further evaluate the generality of our approach, we simulated several variations of the system's geometry by modifying either the magnet height (Fig. 6(a)), the thickness of the mu-metal rings (Fig. 6(b)) or the remanence of the magnet (Fig. 6(c)). As indicated by the dashed black lines, the fit obtained using (1) remains in good agreement with the simulation results for all investigated configurations. This observation even holds when the entire geometry is scaled by a constant factor S_M (Fig. 7a). While the maximum force increases with the magnet volume for constant material properties, the relative positions of the extrema remain unchanged. As a result, the simulated force-displacement curves collapse onto a single characteristic when scaled by the factors S_F and S_z, as shown in Fig. 7(b).

This result implies that the force-displacement behavior of a single mu-metal ring and a magnet can be approximated for optimization purposes using only four parameters: the weighting factors w_1 and w_2, and the Gaussian widths σ_1 and σ_2, which are functions of the design parameters.

Encouraged by this finding, we measured the force-displacement behavior for several combinations of inner and outer diameters (d_in, d_out), limiting ourselves, for now, to those parameters as they can easily be controlled and reproduced. The parameters obtained by fitting (1) to the measured data are presented in Figs. 8 and 9. In these 3D plots, the diameters are represented on the XY-plane, with each point corresponding to one mu-metal ring measurement.

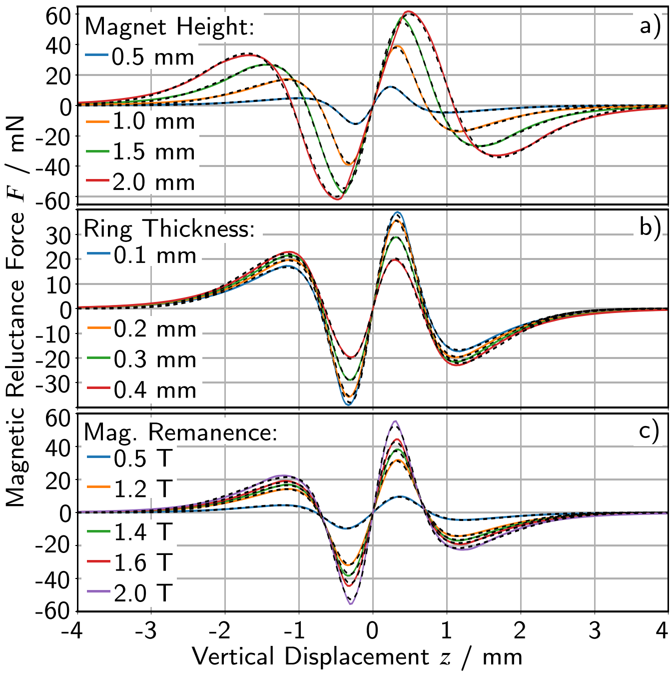

Fig. 6. FEM simulation of other design parameters like magnet height a), thickness of the mu-metal ring b) or remanence of the magnet c). Combined with the fits of function (1), as dashed black lines. Unless otherwise specified in the legends, the remaining design parameters are kept constant at d_{out} = 6.5 mm, d_{in} = 2.7 mm, d_{magnet} = 2 mm, and h_{magnet} = 1 mm. (For interpretation of the references to colour in this figure legend, the reader is referred to the web version of this article.)

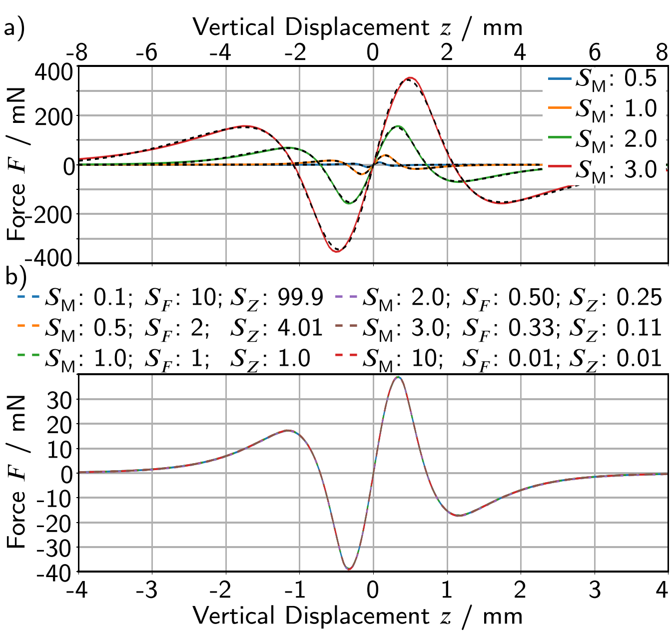

Fig. 7. Simulated force–displacement characteristics a) for different system scaling factors S_M while keeping the material properties constant, together with the corresponding fit using (1). After scaling the force by S_F and the displacement by S_M, all curves collapse onto the same characteristic b).

Fig. 8 shows the weighting factors w_1 and w_2. These factors exhibit a $1/r^2$ dependence on the inner diameter d_{in}, indicating that d_{in} should be chosen as small as possible to maximize the weighting factors and, thereby, the maximum force. In contrast, increasing the outer diameter d_{out} produces only an initial effect. Once a certain threshold is reached, further increases in d_{out} would have only a marginal influence on the weighting factors.

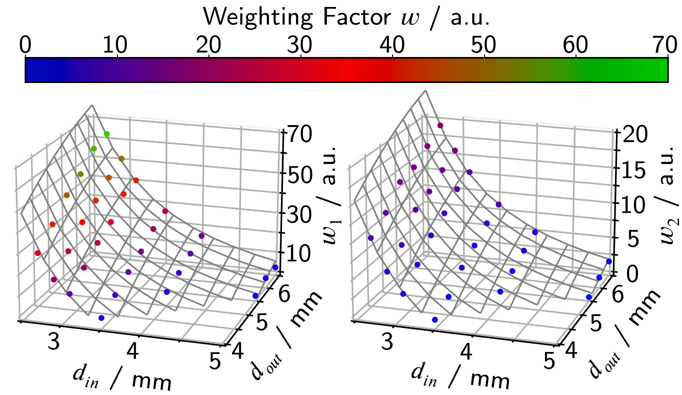

Fig. 8. Weighting factors w_1 (left) and w_2 (right) depending on the inner (d_{in}) and outer (d_{out}) diameters of the mu-metal ring.

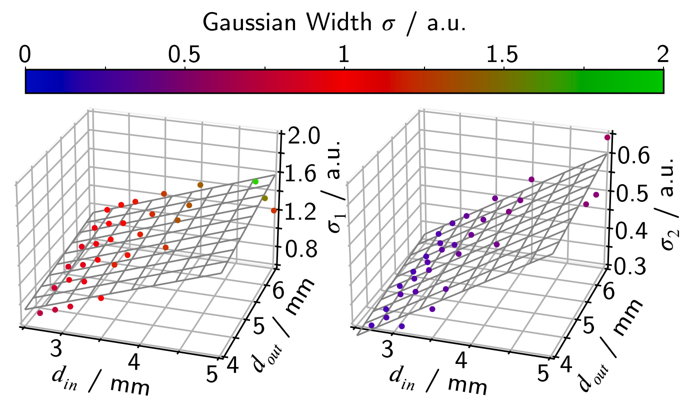

Fig. 9. Gaussian width σ_1 (left) and σ_2 (right) depending on the inner (d_{in}) and outer (d_{out}) diameter of the mu-metal ring.

The Gaussian widths σ_1 and σ_2, on the other hand, display an almost linear, albeit weak, dependence on the mu-metal ring dimensions. This behavior was anticipated based on Fig. 3, where the width of the force–displacement curve remained largely unaffected by changes in diameter, and the same holds true for the two Gaussian widths.

Although the forces can be accurately described by the Gaussian model for a wide range of parameters, it remains an open question to what extent an underlying physical relationship exists. Deriving this formulation from existing numerical or semi-analytical models is challenging and has not yet been achieved. While a thorough investigation is beyond the scope of this work, gaining a deeper understanding of this relationship represents a promising direction for future research, particularly given the scientific value that could arise from a physical interpretation of the Gaussian parameters.

4. Parameter model

As visualized in Figs. 8 and 9, the model parameters follow a deterministic trend depending on the inner and outer diameters. Since the force model (1) is phenomenologically rather than physically motivated, it is challenging to derive a physical relationship between the mu-metal ring and model parameters. However, based on the numerous experimental data, function approximation can be used to obtain an analytical expression that allows interpolation between the known data points. Such a model removes the restriction to a discrete set of predefined rings and increases the flexibility of the actuator design.

To describe each individual Gaussian parameter, we assume models of the form

$$\begin{aligned} \sigma_i &= p_{i,0} + p_{i,1}\, d_{\text{in}} + p_{i,2}\, d_{\text{out}} \\ w_i &= q_{i,0} + \frac{q_{i,1}}{(d_{\text{in}} + q_{i,3})^2} + q_{i,4}(d_{\text{out}} + q_{i,5})^2 \\ i &= 1,2\,. \end{aligned} \tag{2}$$

The model parameters $p_{i,j}$ and $q_{i,j}$ are determined by numerical optimization. However, although the individual parameter models are with principle independent of each other, there is a coupling in regard to the resulting force model. Therefore, it is not sufficient to directly fit the models to the characterized Gaussian parameters. Instead, we simultaneously optimize all parameters so that the deviation between the measured and predicted force is minimized. For this purpose we collect all model parameters $p_{i,j}$, $q_{i,j}$ within the vector $\boldsymbol{p}$ and use the $n_{\text{data}} = 32$ characterized forces $F_{\text{data}}(z)$ to solve the optimization problem

$$\boldsymbol{p}_{\text{opt}} = \arg\min_{\boldsymbol{p}} \sum_{k=1}^{n_{\text{data}}} \int \left(F_{\text{data},k}(z) - F_k(z, \boldsymbol{p}) \right)^2 \mathrm{d}z\,. \tag{3}$$

Note that the integral in (3) is approximated using a rectangular rule. We evaluated the model in terms of the root mean squared error (RMSE) for the data used within the optimization (i.e., the training data), as well as for 10 additional force characteristics not included within the training data (i.e., the validation data). The RMSE was 0.512 mN for the training data and 0.676 mN for the validation data, indicating a sufficient model quality. For comparison, we also optimized the parameter model directly based on the Gaussian parameters, resulting in an RMSE of 1.026 mN for the training data and 1.236 mN for the validation data. This highlights the importance of jointly optimizing the model parameters.

If required, additional parameters such as the ring thickness or permanent magnet dimensions can generally be considered within the model. In this case, the amount of data from measurements or FE simulations should be increased accordingly, and (2) may be replaced by a more general function approximator such as a neural network.

5. Superposition

With the parameters of the single mu-metal rings known, we can now calculate the force-displacement behavior of a multi-ring setup. Our experiments clearly indicate that the overall force can be accurately approximated by the superposition of the single forces, which will be demonstrated in this section.

In a multi-ring system with n_{rings} mu-metal rings, each ring i is physically characterized by its inner and outer diameters $d_{\text{i,in}}$ and $d_{\text{i,out}}$.

With the information gained in Section 3, we can assign a set of model parameters $\boldsymbol{p}_i = [w_{i,1}, w_{i,2}, \sigma_{i,1}, \sigma_{i,2}]$ to each characterized ring to describe the force between the mu-metal ring and the magnet. The force contribution of a single ring at position z_i can be described according to (1) by

$$\begin{aligned} F_i(z) =& w_{i,1} \frac{z - z_i}{\sigma_{i,1}^3 \sqrt{2\pi}} \exp\left(-\frac{1}{2} \left(\frac{z - z_i}{\sigma_{i,1}} \right)^2 \right) \\ & - w_{i,2} \frac{z - z_i}{\sigma_{i,2}^3 \sqrt{2\pi}} \exp\left(-\frac{1}{2} \left(\frac{z - z_i}{\sigma_{i,2}} \right)^2 \right). \end{aligned} \tag{4}$$

The prediction for the overall reluctance force can now be computed by

$$F_{\text{sum}}(z) = \sum_{i}^{n_{\text{rings}}} F_i(z)\,. \tag{5}$$

This process is visualized in Fig. 10 for a set of five identical mu-metal rings with an equal distance of 2.0mm. The gray curves represent each individual function $F_i(z)$ of the five mu-metal rings.

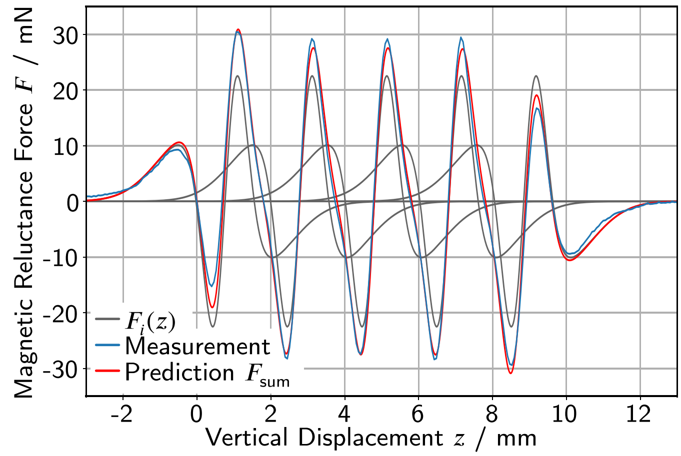

Fig. 10. Graphical representation of the superposition, with each force contribution $F_i(z)$ shown in gray ($i \in \{1, 2, 3, 4, 5\}$). The sum of the contributions forms the prediction F_{sum} represented in red and can be compared to the measurement of an actual actuator. (For interpretation of the references to colour in this figure legend, the reader is referred to the web version of this article.)

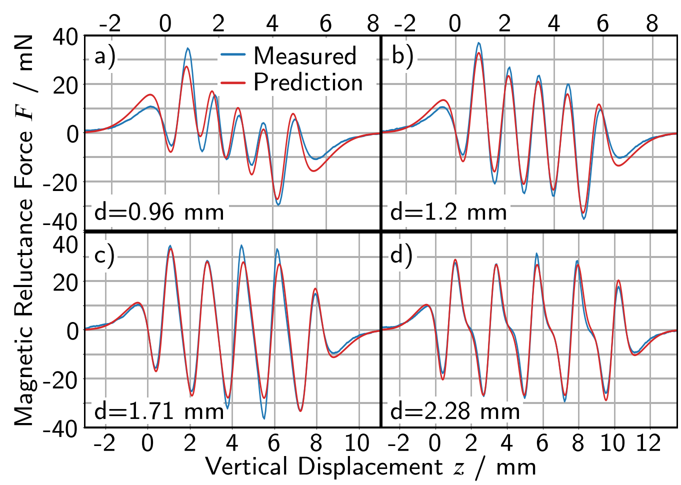

Fig. 11. Predictions and measurements of four actuators with different distances d between the mu-metal rings.

The sum $F_{\text{sum}}(z)$ of the individual functions is plotted in red, representing our force-displacement prediction for such a system, and in blue the actual force measurement done with a physical representation of this setup. Obviously, the prediction and real measurement fit together with a maximum deviation of only 4mN and a correlation of 99.5%.

To validate this superposition method further, we built several actuators with five mu-metal rings, but with varying distances d between the rings. As before, each ring has an inner diameter of 2.7mm and an outer diameter of 6.5mm. The measured force-displacement behaviors for the varying distances are plotted in Fig. 11(a)–(d) (blue), combined with the corresponding predictions obtained by superposition in red.

As shown in the figures, the predictions align closely with the measurements, resulting in correlation values of 95% (a), 98% (b), 99% (c), and 99% (d). Even the saddle-like behavior around the stable positions is predicted correctly for large distances (Fig. 11d).

However, for shorter distances, the discrepancies between predictions and measurements increase, which can be seen by a decrease in correlation by 4%. This is very likely due to saturation effects between the mu-metal rings in close proximity to each other. As expected, the superposition method based on single-ring behavior does not account

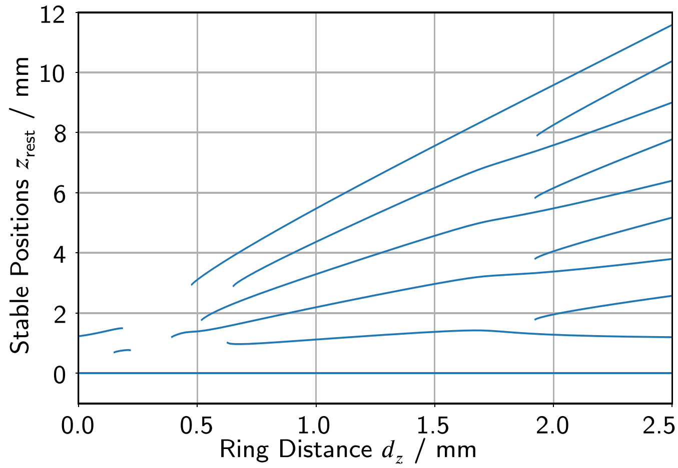

Fig. 12. Bifurcation diagram of the number and locations of stable positions when using 5 mu-metal rings with varying distance d_z.

for this kind of interaction. Still, it remains remarkable that even for this scenario, the number and position of stable points, as well as the upwards drift, are predicted very well. These results indicate that superposition is well-suited to predict the force-displacement behavior for the mu-metal ring reluctance structure of our actuator.

6. Automated actuator design for pre-defined positions

In Section 5, we investigated the force-displacement characteristics corresponding to given configurations of identical, equidistantly positioned mu-metal rings. To obtain application-specific designs, however, we need the inverse approach: Given desired resting positions, we want to know the required types and positions of the mu-metal rings. When the single ring characteristics are known, the superposition principle enables a simulation-based design process. Nevertheless, manually choosing a suitable configuration remains a challenging task due to the strong nonlinearities and the number of design parameters, i.e., the number of rings to be used, their positions and dimensions. To get an impression of the complexity of choosing the optimal design, assume the following simplified scenario: We use 5 identical mu-metal rings with $d_{\text{out}} = 4$ mm, $d_{\text{in}} = 2.7$ mm. Each ring is placed with a distance d_z to its neighboring rings. By varying the distance, we obtain the bifurcation diagram of the resting positions shown in Fig. 12.

Although each ring theoretically provides two stable positions, as described in Section 3, the use of multiple rings does not necessarily lead to a design with $2 \times n_{\text{rings}}$ stable positions.

Instead, the actual number of resting positions can range from only one to twice the number of rings, depending on the distance between the rings. This is due to the fact that for certain distances, the negative force peak of one ring can drastically reduce the positive force peak of the neighboring lower ring. Moreover, the distance between each stable position is non-trivial, which increases the difficulty of manually designing an actuator with predefined locations of stable positions. It is worth mentioning that if a single ring results in only one stable position, for example because small rings are used or the mass of the plunger is high, then the number of stable positions for multiple rings ranges from zero to n_{rings}.

To support the user in finding a suitable setup, we propose numerical optimization to largely automate the design process.

6.1. Numerical optimization

Consider the vector $\boldsymbol{z}^*_{\text{rest}}$ containing the n^*_{rest} desired resting positions in ascending order, where the superscript asterisk will denote user-defined specifications in the remainder of this work.

The goal is to find a configuration of mu-metal rings, such that the sum of forces $F_{\text{sum}}(z)$ at these positions counteracts the plunger's gravitational force and has a negative gradient, i.e.,

$$F_{\text{sum}}(z^*_{\text{rest},k}) = m\,g \tag{6}$$

$$\nabla F_{\text{sum}}(z^*_{\text{rest},k}) < 0 \tag{7}$$

for the k-th desired resting position $z^*_{\text{rest},k}$, the mass m of the plunger, and the gravitational constant g. Mathematically, this can be solved by minimizing a cost function that penalizes both, deviations between the desired and calculated resting positions $\boldsymbol{z}^*_{\text{rest}}$, $\boldsymbol{z}_{\text{rest}}$, and force gradients that exceed a predefined threshold $\nabla F^*_{\max} \leq 0$. In this work, we use a quadratic cost function

$$J = ||\boldsymbol{z}^*_{\text{rest}} - \boldsymbol{z}_{\text{rest}}||_2^2 + w_{\text{grad}}\, c_{\text{grad}}, \tag{8}$$

with the additional gradient penalty term c_{grad} weighted by w_{grad}. This term is only active when the gradient condition is not met, and can be implemented as

$$c_{\text{grad}} = \sum_{k=1}^{n^*} \left(\nabla F_{\text{sum}}(z^*_{\text{rest},k}) - \nabla F^*_{\max}\right)^2 \times \begin{cases} 1 \text{ if } \nabla F_{\text{sum}}(z^*_{\text{rest},k}) > \nabla F^*_{\max} \\ 0 \text{ otherwise}\,. \end{cases} \tag{9}$$

Besides stability and accuracy of the resting positions, robustness is typically an important design criterion. If the force or energy barrier beside a resting position is low, external disturbances can lead to an unwanted transition to the neighboring resting position. This can be prevented by increasing the force peaks $\boldsymbol{F}_{\text{peak}}$ between the resting positions. To tune this force barrier, an additional penalty term c_{peak} is added to the cost function, which penalizes peak forces that are lower than a given value F^*_{peak}.

We use a similar formulation as for the gradient penalty in (9), resulting in the term

$$c_{\text{peak}} = \sum_{k=1} \left(F_{\text{peak},k} - F^*_{\text{peak}}\right)^2 \times \begin{cases} 1 \text{ if } F_{\text{peak},k} < F^*_{\text{peak}} \\ 0 \text{ otherwise}\,. \end{cases} \tag{10}$$

The predicted resting positions $\boldsymbol{z}_{\text{rest}}$, gradients $\nabla F_{\text{sum}}(z^*_{\text{rest},k})$, and force peaks $\boldsymbol{F}_{\text{peak}}$ needed to calculate the cost function are evaluated numerically depending on the ring types and positions.

For each ring, three parameters, namely the inner and outer diameters, as well as its position, need to be optimized. Instead of optimizing the positions z_i of each ring directly, we choose the distances d_i between the rings as optimization parameters, while the first optimal ring position z_1 will later be set automatically. The position of the i-th ring is then given by

$$z_i = z_{i-1} + d_i + h_{\text{ring}}, \; i = 2, \ldots, n_{\text{rings}}, \tag{11}$$

where h_{ring} is the thickness of a single ring. This formulation has several advantages: On the one hand, it simplifies the implementation of constraints to avoid infeasible designs, for example due to overlapping mu-metal rings. On the other hand, this enables the use of a discrete set Λ of available FR2-spacer widths, since realizing arbitrarily accurate spacers may be unrealistic. We construct the discrete set Λ by considering two available spacer thicknesses (0.32 mm and 0.5 mm) and generating all possible linear combinations of spacers up to a maximum of 2 mm.

Regarding the ring dimensions, we propose two different strategies: The first option is to use only the ring types that have been evaluated in experiments.

In our case, 32 different types with inner diameters $d_{\mathrm{in}} \in [2.7, 5.0]$ mm and outer diameters $d_{\mathrm{out}} \in [4.0, 6.5]$ mm are considered. To allow the algorithm to select no ring at certain locations, we extend the number of rings by a parameter set with zero weighting factors denoted as zero-ring. This discrete approach is particularly useful if only the parameters of few mu-metal rings are available.

The second option is to directly optimize the diameters in terms of continuous variables, exploiting the parameter model (2) discussed in Section 4. The advantage lies in its high flexibility in choosing the optimal ring types, increasing the accuracy of the resulting resting positions. However, a higher number of characterized rings is required for fitting the parameter model to ensure a sufficient approximation quality. It is important to mention that this formulation allows for the selection of infeasible combinations (e.g., $d_{\mathrm{in}} > d_{\mathrm{out}}$) if it is not constrained properly. Rather than using additional constraints, we exploit this to include zero-rings for each combination that would otherwise be infeasible.

For both strategies, we summarize the available ring types defined as $\boldsymbol{R}_i = [d_{\mathrm{i,in}}, d_{\mathrm{i,out}}]$ in the set Γ_{d}.

The overall optimization problem is then formulated as the constrained nonlinear integer program

$$\begin{aligned} \min_{\boldsymbol{R}_i, d_i} \; & ||\boldsymbol{z}^*_{\mathrm{rest}} - \boldsymbol{z}_{\mathrm{rest}}||_2^2 + w_{\mathrm{grad}}\, c_{\mathrm{grad}} + w_{\mathrm{peak}}\, c_{\mathrm{peak}} \\ \text{s.t.} \; & \boldsymbol{R}_i \in \Gamma_{\mathrm{d}}, \quad i = 1, \dots, n_{\mathrm{rings}} \\ & d_i \in \Lambda, \quad i = 2, \dots, n_{\mathrm{rings}} . \end{aligned} \tag{12}$$

Some further computations are required to evaluate the cost function, namely the force peaks, the coordinates of the resting positions, and the location z_1 of the first ring. The predicted resting positions and force peaks are determined numerically using a grid search, since there is no analytical solution.

Changing the first ring position corresponds to a shift of the entire force-displacement curve in z. Thus, we can choose z_1 in such a way that the average quadratic error between $\boldsymbol{z}^*_{\mathrm{rest}}$ and $\boldsymbol{z}_{\mathrm{rest}}$ is minimized for given ring types $\boldsymbol{R}_i$ and distances d_i.

To achieve this, we first compute F_{sum} for $z_1 = 0$ mm and evaluate the resulting locations of stable positions, which we denote as $\boldsymbol{z}^0_{\mathrm{rest}}$. The resting positions are then given by

$$\boldsymbol{z}_{\mathrm{rest}} = \boldsymbol{z}^0_{\mathrm{rest}} + z_1 . \tag{13}$$

To obtain the optimal z_1, we solve the minimiztion problem

$$z_{1,\mathrm{opt}} = arg\, min_{z_1} ||\boldsymbol{z}^*_{\mathrm{rest}} - (\boldsymbol{z}^0_{\mathrm{rest}} + z_1)||_2^2, \tag{14}$$

which yields the analytic solution

$$z_{1,\mathrm{opt}} = \frac{1}{n^*_{\mathrm{rest}}} \sum_{k=1}^{n^*_{\mathrm{rest}}} (z^*_{\mathrm{rest},k} - z^0_{\mathrm{rest},k}) . \tag{15}$$

This can be inserted into our original problem (12).

Finally, we discuss two special cases that need to be considered in our algorithm. As visualized in Fig. 12, the number of predicted stable positions can vary depending on the chosen parameters. Therefore, the cost function needs to be well-defined even if the number of resting positions differs from the desired ones. In case where fewer resting positions are predicted, z_1 is chosen such that the deviations of the lowest stable positions are minimized. A constant penalty is added to the cost function for each missing one. If the predicted number of stable positions exceeds that of the desired ones, the best fitting combination of predicted positions is selected.

We want to mention that this algorithm could in general also be implemented using alternative force models, or directly within FEM software. However, this strategy depends on a global optimizer that can handle nonlinear integer or mixed integer problems, which typically leads to a large number of function evaluations. Therefore, the limiting factor remains the required time to calculate a single force-displacement characteristic, which should lie in the range of milliseconds. So far, this is only achieved with our proposed phenomenological Gaussian model.

7. Results

In the following we demonstrate the effectiveness of using the superposition principle for an automated design based on optimization. Moreover, we highlight the limitations of the accuracy of the resting positions depending on the desired distance between them.

For this purpose, we allow the algorithm to use up to $n_{\mathrm{rings}} = 4$ mu-metal rings to obtain $n^*_{\mathrm{rest}} = 4$ equidistant resting positions $\boldsymbol{z}^*_{\mathrm{rest}}$ with specified distances. The results will be evaluated in terms of the mean absolute error (MAE) between the desired and obtained resting positions, i.e.,

$$\mathrm{MAE} = \frac{1}{n^*_{\mathrm{rest}}} \sum_{k=1}^{n^*_{\mathrm{rest}}} |z^*_{\mathrm{rest},k} - z_{\mathrm{rest},k}|, \tag{16}$$

as well as its maximum deviation

$$e_{\max} = \max_k \; |z^*_{\mathrm{rest},k} - z_{\mathrm{rest},k}| . \tag{17}$$

Moreover, we investigate how varying the desired minimum force peak F^*_{peak} affects the accuracy of the resting positions and the actual minimum force barrier $\min \boldsymbol{F}_{\mathrm{peak}}$.

The optimization is solved in MATLAB using the genetic algorithm [27] and we manually tuned the weighting coefficient $w_{\mathrm{peak}} = 4 \times 10^{-4}$ to find a suitable compromise between resting position accuracy and achieved minimum force. In the following experiments, we set $\nabla F^*_{\max} = 0N/m$, i.e., we do not specify an additional minimum stiffness of the resting positions. Thus, the weighting coefficient w_{grad} does not influence the results. The effect of this additional robustness parameter will be briefly investigated later in this work. It is important to mention that all calculations within the cost function are performed with the units mN and mm. If other prefixes are used, the weighting factors need to be adjusted accordingly. Due to the high nonlinearity of the problem, the optimization may converge to a different solution in each run. Therefore, the algorithm was executed 10 times for each experiment, and the best result according to the cost function (12) was selected.

7.1. Optimal designs

We first demonstrate the applicability of the optimization-based design approach by generating designs according to different specifications and subsequently verifying them in real experiments. We conducted experiments for 3 different sets of desired equidistant resting positions $\boldsymbol{z}^*_{\mathrm{rest}} = [0, 1, 2, 3] \cdot \Delta z^*_{\mathrm{rest}}$ with distances $\Delta z^*_{\mathrm{rest}} \in \{1.0, 1.3, 1.6\}$ mm. To investigate the effect of the minimum force barrier, we chose different references $F^*_{\mathrm{peak}} \in \{0, 10, 20\}$ mN. For comparison, we optimized all design variations selecting mu-metal rings either from a discrete set of predefined ring types $\boldsymbol{R}_i$ (in the following denoted as *discrete*) or from a continuous set using the parameter model (2) (denoted as *continuous*).

The results are summarized in Table 1 and show high accuracy of the resting positions in both simulation and experiments. In simulation, the accuracy slightly decreases for higher values of the desired force barrier in most cases. This is due to the fact that the weighting factor w_{peak} in the cost function trades off accuracy against robustness. The only exception to this observation is the experiment with discrete rings and $\Delta z^*_{\mathrm{rest}} = 1.3$ mm, $F^*_{\mathrm{peak}} = 10$ mN, which has a smaller average error than for $F^*_{\mathrm{peak}} = 0$ mN despite its higher minimum peak force. We would expect that the most accurate results are exclusively obtained without requirements on the force barrier. The reason why this is not the case lies in the complexity and nonlinearity of the optimization problem.

The experiments also show sufficiently accurate results, although their accuracy and robustness decrease in comparison to the predicted results. Reasons for this observation include approximation errors, but also variations with the fabricated mu-metal rings and spacers, particularly in regard to their thickness. As expected, the results can be improved when the choice of the mu-metal rings is not limited to a discrete set. By using the continuous parameter model for the design

Table 1
Experimental validation of optimized designs with discrete and continuous ring dimensions.

Desired design		Numerical results (discrete)			Experimental results (discrete)			Numerical results (continuous)			Experimental results (continuous)		
Δz^*_{rest} [mm]	F^*_{peak} [mN]	MAE [μm]	$e_{\max}$ [μm]	min F_{peak} [mN]	MAE [μm]	$e_{\max}$ [μm]	min F_{peak} [mN]	MAE [μm]	$e_{\max}$ [μm]	min F_{peak} [mN]	MAE [μm]	$e_{\max}$ [μm]	min F_{peak} [mN]
1.0	0	3.17	5.76	2.21	31.44	62.13	1.71	0.12	1.87	3.03	32.08	65.61	1.39
1.0	10	13.35	17.04	9.36	32.35	55.23	4.54	1.71	2.99	10.78	28.92	52.88	12.06
1.0	20	52.51	68.86	18.66	63.73	95.81	16.53	10.68	21.11	17.25	32.25	55.73	14.83
1.3	0	1.71	3.02	3.95	37.22	57.52	3.47	0.03	1.53	10.43	36.06	62.35	9.43
1.3	10	1.10	1.72	11.94	39.44	62.10	9.61	0.14	1.23	10.15	52.60	58.77	12.23
1.3	20	12.48	24.17	18.47	35.46	56.27	16.37	5.28	12.28	18.08	17.87	25.26	16.11
1.6	0	1.01	1.54	7.46	31.36	62.71	8.90	0.05	1.07	6.57	29.07	50.19	6.32
1.6	10	2.46	3.86	10.86	60.36	73.41	10.87	2.18	3.39	11.32	20.09	31.11	11.88
1.6	20	31.38	42.68	16.68	37.74	75.49	15.68	11.07	22.01	15.60	19.24	28.88	16.63

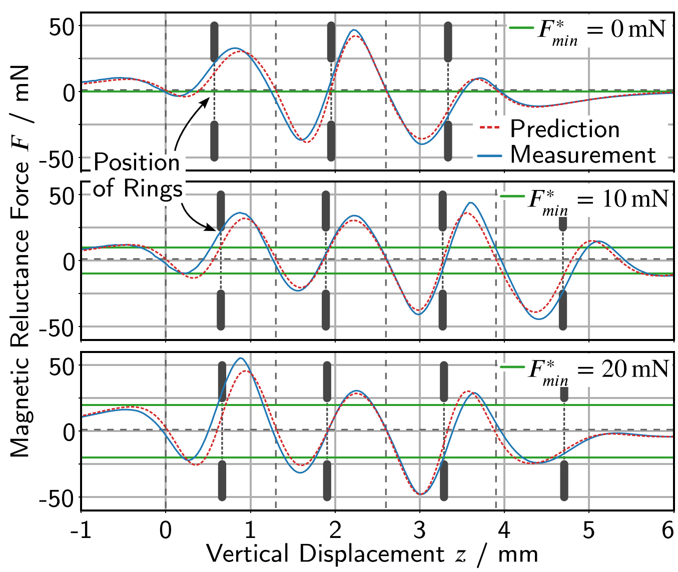

Fig. 13. Optimization results using a discrete set of mu-metal rings for the desired resting position distance $\Delta z^*_{\text{rest}} = 1.3$ mm and different minimum force references $F^*_{\text{peak}} \in \{0, 10, 20\}$ mN. The prediction (dashed, red) and measurement (solid, blue) are compared. The desired resting positions are marked as gray vertical lines. The gravitational force is depicted as dashed line. (For interpretation of the references to colour in this figure legend, the reader is referred to the web version of this article.)

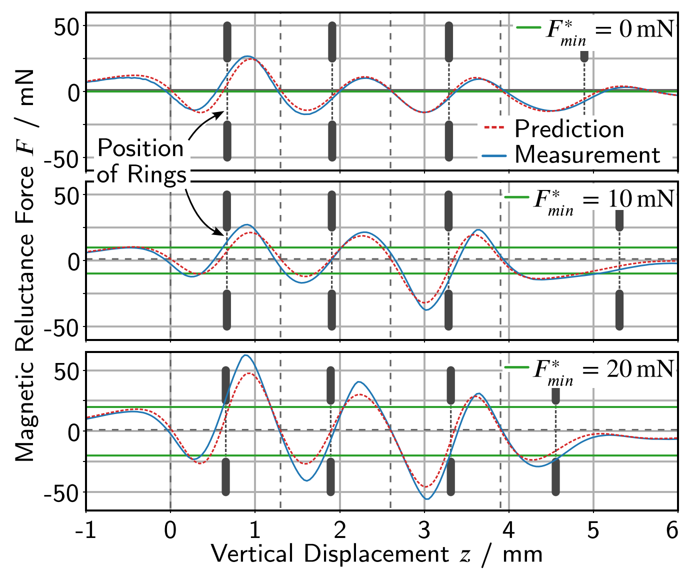

Fig. 14. Optimization results using the continuous parameter model for the mu-metal rings, with the desired resting position distance $\Delta z^*_{\text{rest}} = 1.3$ mm and different minimum force references $F^*_{\text{peak}} \in \{0, 10, 20\}$ mN. The prediction (dashed, red) and measurement (solid, blue) are compared. The desired resting positions are marked as gray vertical lines. The gravitational force is depicted as dashed line. (For interpretation of the references to colour in this figure legend, the reader is referred to the web version of this article.)

optimization, the accuracy increases in almost all cases in both simulation and experiment. However, no particular improvement is apparent in terms of robustness.

We visualized the series of experiments with $\Delta z^*_{\text{rest}} = 1.3$ mm in Fig. 13 for the discrete case and Fig. 14 for the continuous case. These experiments are selected because of two special features apparent in the discrete case (Fig. 13). The experiment with $F^*_{\text{peak}} = 0$ mN only uses three rings to generate the four resting positions, while the other experiments contain four rings. In this case, the topmost ring was eliminated by the optimization. Moreover, the experiment according to $F^*_{\text{peak}} = 10$ mN yields an additional, but unused resting position around 5.3 mm. Here, the first four resting positions were chosen due to a lower cost function value.

In general, a larger number of rings adds additional degrees of freedom in the design and allows for a more accurate adjustment of the resting positions as well as higher robustness. The latter can be seen in particular when comparing the 4th resting position of the first two experiments in Fig. 13. The force barrier of the first experiment ($F^*_{\text{peak}} = 0$ mN), which only uses three rings, is relatively low, whereas the additional ring in the second experiment ($F^*_{\text{peak}} = 10$ mN) drastically increases this force barrier.

Comparable results are obtained when the mu-metal ring dimensions are selected from a continuous set, as seen in Fig. 14. The optimization yields different ring sizes and positions than in Fig. 13, leading to different force–displacement curves. Small improvements can be observed in the continuous case. However, this improvement is only subtle in the graphical representation and becomes clearer when comparing the results in Table 1.

7.2. Limitations

Besides the fact that the accuracy decreases with higher demands on robustness, Table 1 reveals another relevant observation: The predicted design quality depends on the desired distance between the resting positions and appears to be optimal for values close to $\Delta z^*_{\text{rest}} = 1.3$ mm. To investigate its effect on the error and attainable force barrier, we numerically generated optimal designs with varying distances Δz. To obtain the most general assessment of the theoretically possible accuracy, we allowed the optimization algorithm to use continuous values for both the ring dimensions and the spacers. As before, the simulative study was conducted with varying requirements on the minimum force barrier. The results are shown in Fig. 15.

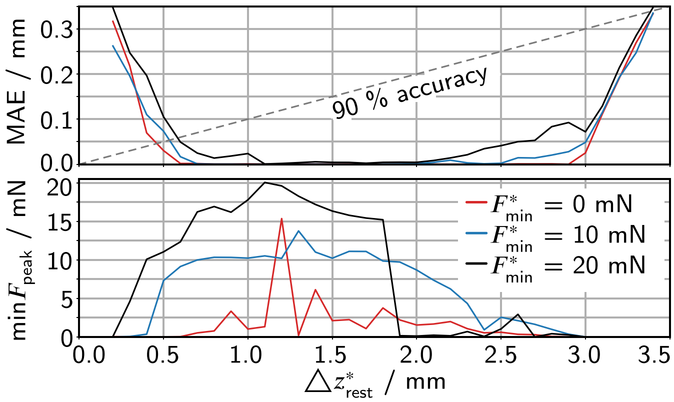

Fig. 15. Accuracy and robustness in terms of the MAE and the minimum force barrier depending on the distance Δz^*_{rest} between the resting positions. Limitations can be observed for both small and large distances. The results below the 90% accuracy line have an MAE of less than 10% of the desired distance.

We can observe strong limitations in the accuracy when either very small (< 0.5 mm) or large distances (> 3.0 mm) between the resting positions are desired.

For example, an MAE of less than 10% can only be achieved for a minimum distance of approximately 0.45 mm – 0.6 mm depending on the specifications of the minimum force barrier. A high accuracy can be achieved up to a distance of approximately 3.0 mm. Beyond this point, the MAE increases and intersects the 90% accuracy line at approximately 3.4 mm. However, the limiting factor for larger distances is the rapidly decreasing peak force starting at approximately 1.8 mm. A compromise between accuracy and robustness is evident mostly at the lower bound: higher accuracy for small distances can be achieved when the requirements on the force barrier F^*_{peak} are low. The force barrier in case of $F^*_{\text{peak}} = 0$ mN has no meaningful significance and is included in the figure only for the sake of completeness. However, it illustrates that in general, lower force peaks occur when the focus solely lies on accuracy.

To explain the lower and upper limits of the attainable resting position distance, we recall several observations: First, to adjust the resting positions, we make extensive use of the superposition of forces corresponding to single mu-metal rings, thereby increasing or decreasing the overall force depending on their relative displacements. Secondly, small distances between the resting positions also require the rings to be closer together, and vice versa.

In the following, we visualize the limiting physical effects with an example involving two identical mu-metal rings, symmetrically arranged around the zero position. As seen in Fig. 16(a), if the rings become too close, previously stable intermediate positions become weaker, i.e., the force barrier decreases. When reducing the distance even further, the gradient at this position starts to switch its sign, replacing the stable resting position with an unstable one. This effect can also be observed for distances smaller than 0.7 mm in the bifurcation diagram in Fig. 12 which limits the minimum achievable resting position distance.

The opposite effect is observed when increasing the distance between the rings when starting at a larger initial distance; see Fig. 16(b). We again start with three resting positions with identical distances. When the rings are moved farther apart, the stable intermediate position also becomes weaker, and eventually unstable. At this point, two new stable resting positions with low force barriers occur, but instead of the intended increase in the resting position distance, the new second and third positions are now closer together than before. This is also illustrated in the bifurcation diagram Fig. 12 around 1.9 mm. The first and second pair of resting positions now correspond mostly unchanged to the two resting positions of the single mu-metal rings, which are fixed by the choice of the rings. Therefore, further moving the rings apart only changes the distance between the second and third resting positions, setting a limit to the upper achievable resting position distance. Both limiting effects can, to some extent, be delayed but not fully prevented by changing the ring dimensions.

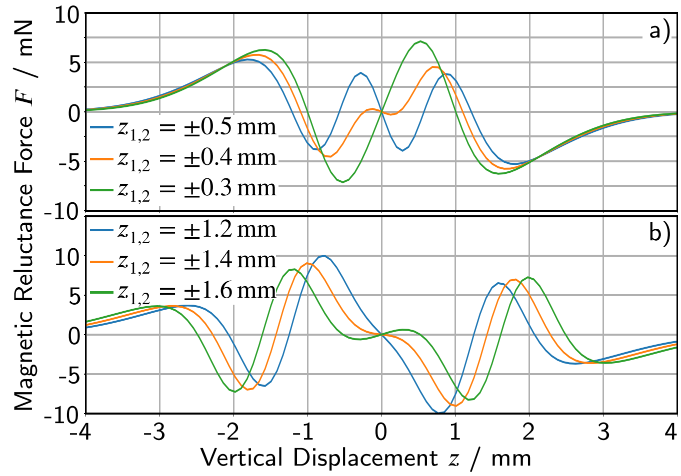

Fig. 16. Overall force corresponding to a setup with two identical, symmetrically arranged mu-metal rings with varying distances between them to analyze the physical reasons for the limitations. a) Decreasing the small distance between the rings can lead to the cancellation of intermediate stable resting positions. b) Increasing the distance beyond a critical point leads to a sudden increase in resting positions.

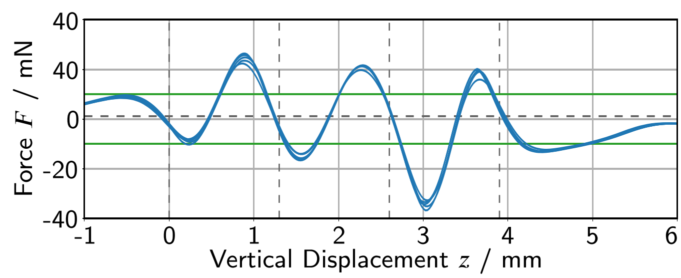

Fig. 17. Force-Displacement curves for 5 individually fabricated setups according to the same mu-metal ring configuration optimized for $\Delta z^*_{\text{rest}} = 1.3$ mm, $F^*_{\text{peak}} = 10$ mN. The small variance between the results indicates sufficient robustness against fabrication tolerances.

8. Discussions

The presented results clearly demonstrate the applicability of our approach while outlining the current limitations. In this section, we aim to discuss further aspects that become particularly relevant for practical applications.

8.1. Robustness against Fabrication Tolerances

As is typical for numerical design approaches, our optimization algorithm relies on accurate models and does not take into account fabrication tolerances. It is therefore important to investigate the robustness of the solution against fabrication tolerances and small assembly errors. In our case, variations in the resulting force-displacement curves can be caused, for example, by variances in the mu-metal ring dimensions and spacer widths or by slight misplacement of the rings.

To provide a realistic assessment in a practical scenario, we produced 5 setups according to identical configurations of mu-metal rings. The chosen scenario corresponds to the case $\Delta z^*_{\text{rest}} = 1.3$ mm, $F^*_{\text{peak}} = 10$ mN and the results are shown in Fig. 17.

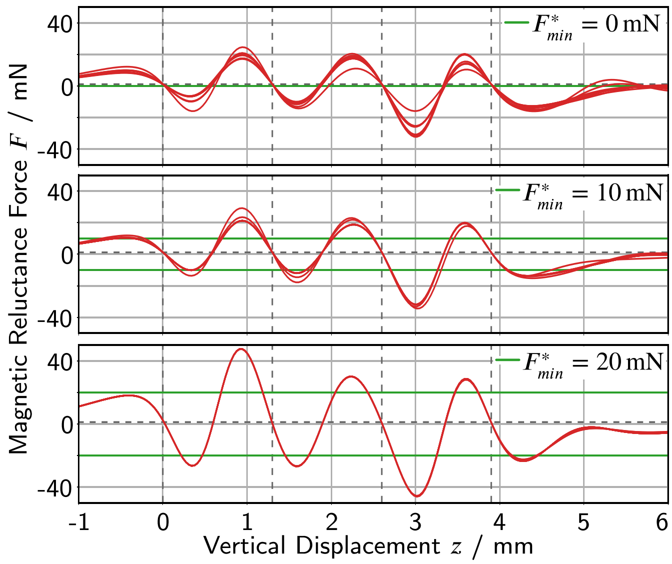

Fig. 18. Repeatability of the optimization results for the experiments shown in Fig. 14. The predicted force-displacement curves of 10 independent optimization runs for each experiment are shown. Larger variations can be observed for lower minimum force references F^*_{peak}, although robustness and resting position accuracy are only marginally.

It is important to mention that the assembly was done manually without precision tools. Nevertheless, the results indicate a satisfactory robustness even under non-ideal conditions. Particularly the design goals, i.e., the accuracy and minimum force peak, seem to be affected only marginally with an MAE of 52.5 µm and a standard deviation of 12.6 µm for the accuracy, and an average minimum peak force of 8.80 mN with a standard deviation of 0.636 mN.

The main variation is seen in the higher force peaks. We assume that the reason for this is that the maximum force has the highest sensitivity with respect to the positioning of the rings, but it may also be more affected by variations in the ring dimensions than the smaller peaks. Especially when the higher force peaks are critical for an application, a more precise automated process would be beneficial to further increase the robustness and reliability.

8.2. Repeatability of the optimization

Due to the stochastic nature of the genetic algorithm, it may still converge to different solutions in each run when multiple local minima exist, even though it is considered a global optimizer. For our approach to be practically applicable, we require reproducible results, or at least demand that the requirements are satisfied to a comparable extent in each run. To investigate the variance of the results, we compared the predicted force-displacement characteristics of all 10 runs for the cases $\Delta z^*_{rest} = 1.3$ mm, $F^*_{peak} \in \{0, 10, 20\}$ mN. This is visualized in Fig. 18.

We define our optimization procedure as highly repeatable, if there is only small variance in the achieved design goals, i.e., the resting position accuracy and minimum force barrier. The evaluated standard deviation of the MAE and minimum force barrier, together with their mean values, are given in Table 2 for the results shown in Fig. 18.

It can be seen that the variance of both the MAE and minimum force barrier is low throughout all cases, with exception of the minimum force barrier in case of $F^*_{peak} = 0$ mN. However, this is acceptable as there was no requirement for robustness. Based on these results, we conclude that our algorithm produces sufficiently reliable results, although the exact solution may vary. As a single optimization run took only an average of 302 s without parallelization, we nevertheless recommend running the algorithm multiple times and subsequently choosing the best result.

Table 2
Mean and standard deviation of the resting position accuracy and minimum force peaks for multiple optimization runs.

F^*_{peak} [mN]	μ(MAE) [µm]	σ(MAE) [µm]	$\mu(F_{peak})$ [mN]	$\sigma(F_{peak})$ [mN]
0	0.18	0.073	7.9	1.8
10	0.21	0.084	10.3	0.55
20	5.3	0.034	18.1	0.0015

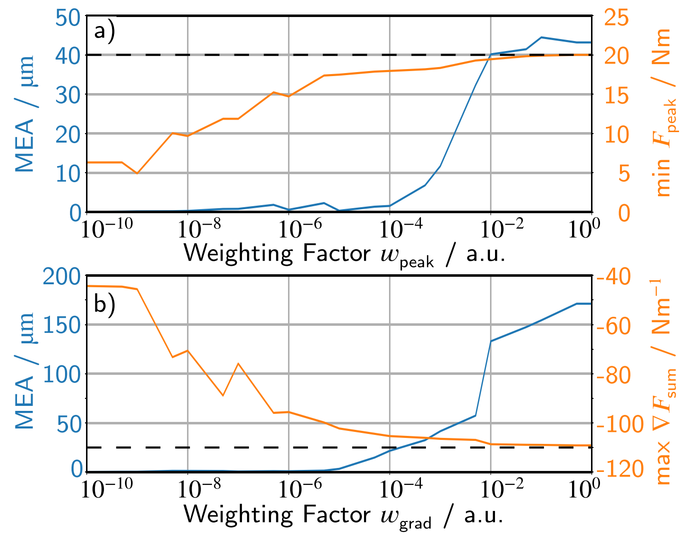

Fig. 19. Effect of the weighting factors w_{peak} a) and w_{grad} b) on the optimization results with $\Delta z^*_{rest} = 1.3$ mm, when the other weighting factor is set to zero. The dashed line corresponds to the desired minimum peak force $F^*_{peak} = 20$ mN and maximum force gradient $\nabla F^*_{sum} = -110$ N/m, respectively.

8.3. Weighting parameter sensitivity

So far, we have assumed a fixed pair of manually tuned weighting parameters w_{peak}, w_{grad} within our optimization algorithm. However, a more detailed investigation of the effect and sensitivity of these parameters can provide valuable insights for making a well-founded compromise between resting position accuracy and robustness.

For this purpose, we repeated the optimization for $\Delta z^*_{rest} = 1.3$ mm and varied one weighting parameter over a large range, while setting the other one to zero. For the minimum peak force and the maximum gradient, we chose $F^*_{peak} = 20$ mN and $\nabla F^*_{sum} = -110$ N/m, respectively, which were found to be values at the limits of what is achievable in this case. The results are shown in Fig. 19.

While the range of suitable weighting parameters strongly depends on the user's priorities, the analysis allows one to define an approximate parameter range from which a subsequent manual fine-tuning can be performed. We recommend initializing the peak force weighting parameter within the range $w_{peak} \in [10^{-5}, 10^{-3}]$, and the gradient parameter within $w_{grad} \in [10^{-6}, 10^{-4}]$.

9. Conclusion

We demonstrated that the reluctance force between a cylindrical permanent magnet and a mu-metal ring can be sufficiently described by a phenomenological model with only 4 parameters. So far, this model can be fitted to the force–displacement characteristics for a large variety of ring dimensions with high accuracy, and no limitations have yet been identified. In contrast to common semi-analytical or numerical models, the evaluation time is drastically reduced by up to a factor of 1.7×10^4 compared to established models [24].

One of the main contributions of this work is the experimental verification of the superposition principle to approximate the force-displacement curves of multi-ring configurations based on the force contribution of single rings. Such an analytical approach allows for a fast simulation-based analysis and design without the need for computationally expensive numerical approaches.

This makes the model particularly suitable for an automated design using numerical optimization. For this purpose, we proposed an optimization framework that generates suitable designs based on requirements on the number and locations of resting positions, as well as the desired force barrier to achieve a certain robustness. Both numerical and experimental results confirm the effectiveness of the presented strategy to generate application-specific actuator designs.

The achievable accuracy of the setup depends mainly on two aspects, namely the accuracy of the analytical approximation, and the desired distance between the resting positions. The approximation quality is limited by fabrication tolerances and neglected coupling effects, which may be further investigated in future work. A current limitation is that resting positions with too little or too much distance are infeasible with the magnet and mu-metal ring dimensions used in this work. However, we showed in a brief numerical study that adjusting the length of the permanent magnet and the ring thickness has a considerable effect on the force-displacement characteristic. This could be used in future work to reduce the current limitations.

The described multistable actuator may serve in applications such as optical multiplexing [28], piston motion mirrors [29], or multistable valves [30]. As demonstrated in [31], multistable actuators with linear displacement are also advantageous in microrobotics, although our system would benefit from further miniaturization.

The field of applications may also be extended if the switching between the resting positions could be induced by external magnetic fields. While such scenarios are common for medical applications as in [32], this can also benefit other fields such as microrobotics [33]. For this purpose, future research should investigate the effect of external magnetic loading on the force-displacement curves to validate our Gaussian model's generalizability.

CRediT authorship contribution statement

Pascal M. Weber: Writing – original draft, Validation, Software, Methodology, Investigation, Formal analysis, Conceptualization. **Michael Olbrich:** Writing – original draft, Software, Methodology, Formal analysis, Conceptualization. **Yannik T. Rüde:** Investigation, Data curation. **Christoph Ament:** Writing – review & editing, Supervision, Funding acquisition. **Ulrike Wallrabe:** Writing – review & editing, Supervision, Funding acquisition.

Declaration of competing interest

The authors declare the following financial interests/personal relationships which may be considered as potential competing interests:

Pascal Manuel Weber reports that financial support was provided by German Research Foundation. Michael Olbrich reports that financial support was provided by German Research Foundation. If there are other authors, they declare that they have no known competing financial interests or personal relationships that could have appeared to influence the work reported in this paper.

Acknowledgements

This research was funded by the German Research Foundation (DFG) within the priority program SPP2206 "KOMMMA", project "ADOPT - Adaptive Optics for THz", grant number 424616052.

The authors also want to thank Arwed Schütz for his support regarding finite element modeling.

Data availability

Data will be made available on request.

References

[1] X. Chen, L. Bumke, E. Quandt, M. Kohl, Bistable actuation based on antagonistic buckling SMA beams, Actuators 12 (11) (2023), https://doi.org/10.1007/s00542-024-05652-9
[2] L. Petit, C. Prelle, E. Doré, F. Lamarque, M. Bigerelle, A four-discrete-position electromagnetic actuator: modeling and experimentation, IEEE/ASME Trans. Mechatron. 15 (1) (2009) 88–96, https://doi.org/10.1109/TMECH.2009.2017018
[3] I. Bouhadda, A. Mohand-Ousaid, G. Bourbon, P. Le Moal, P. Lutz, H. Hussein, Y. Haddab, Repeatability and reproducibility analysis of a multistable module devoted to digital microrobotics, in: IEEE/RSJ International Conference on Intelligent Robots and Systems (IROS), 2018, pp. 4889–4894, https://doi.org/10.1109/IROS.2018.8594259
[4] H. Hussein, H. Fariborzi, Accurate sensorless multistable microsystem with a single actuator, Front. Mech. Eng. 8 (2022), https://doi.org/10.3389/fmech.2022.825470
[5] A. Crivaro, R. Sheridan, M. Frecker, T.W. Simpson, P. Von Lockette, Bistable compliant mechanism using magneto active elastomer actuation, J. Intell. Mater. Syst. Struct. 27 (15) (2016) 2049–2061, https://doi.org/10.1177/1045389X15620037
[6] S.W. Huang, F.C. Lin, Y.J. Yang, A novel single-actuator bistable microdevice with a moment-driven mechanism, Sens. Actuators A Phys. 310 (2020), https://doi.org/10.1016/j.sna.2020.111934
[7] J.S. Han, C. Müller, U. Wallrabe, J.G. Korvink, Design, simulation, and fabrication of a quadstable monolithic mechanism with X-and Y-directional bistable curved beams, J. Mech. Des. 129 (11) (2007) 1198–1203, https://doi.org/10.1115/1.2771577
[8] C. Goll, W. Bacher, B. Büstgens, D. Maas, W. Menz, W.K. Schomburg, Microvalves with bistable buckled polymer diaphragms, J. Micromech. Microeng. 6 (1) (1996) 77–79, https://doi.org/10.1088/0960-1317/6/1/017
[9] X. Miao, X. Dai, G. Ding, X. Zhao, Simulation and fabrication of a bistable electromagnetic micro-actuator, Electromagnetics 32 (5) (2012) 274–286, https://doi.org/10.1080/02726343.2012.686836
[10] X. Wang, C. Zhi, Y. Li, M. Qu, Z. Xiong, Design and analysis of micro inertial switch with magnetic latch and adjustable threshold, Microsyst. Technol. 30 (8) (2024) 1039–1048, https://doi.org/10.1007/s00542-024-05652-9
[11] X.Q. Li, W.B. Li, W.M. Zhang, H.X. Zou, Z.K. Peng, G. Meng, Magnetic force induced tristability for dielectric elastomer actuators, Smart Mater. Struct. 26 (10) (2017), https://doi.org/10.1088/1361-665X/aa8282
[12] H. Hussein, F. Khan, M.I. Younis, A monolithic tunable symmetric bistable mechanism, Smart Mater. Struct. 29 (7) (2020), https://doi.org/10.1088/1361-665X/ab8ea3
[13] W.K. Schomburg, C. Goll, Design optimization of bistable microdiaphragm valves, Sens. Actuators A Phys. 64 (3) (1998) 259–264, https://doi.org/10.1016/S0924-4247(97)01612-9
[14] P.M. Weber, U. Wallrabe, Cantilever free multistable magnetic lift actuator for large out-of-plane displacements, in: 23rd International Conference on Solid-State Sensors, Actuators and Microsystems (Transducers), 2025, pp. 600–603, https://doi.org/10.1109/Transducers61432.2025.11110839
[15] K. Fuchi, T.H. Ware, P.R. Buskohl, G.W. Reich, R.A. Vaia, T.J. White, J.J. Joo, Topology optimization for the design of folding liquid crystal elastomer actuators, Soft Matter 11 (37) (2015) 7288–7295, https://doi.org/10.1039/c5sm01671a
[16] L.Y. Ma, A.N. Nordin, N. Soin, Design, optimization and simulation of a low-voltage shunt capacitive RF-MEMS switch, Microsyst. Technol. 22 (3) (2016) 537–549, https://doi.org/10.1007/s00542-015-2585-5
[17] B. Liu, V. Grout, A. Nikolaeva, Efficient global optimization of actuator based on a surrogate model assisted hybrid algorithm, IEEE Trans. Ind. Electron. 65 (7) (2017) 5712–5721, https://doi.org/10.1109/TIE.2017.2782203
[18] B. Parsi, A. Abouzarkhanifard, L. Zhang, Design and optimization of piezoelectric actuators for microflap-embedded micropumps, Adv. Mech. Eng. 15 (5) (2023) 1–12, https://doi.org/10.1177/16878132231158983
[19] J. Hey, T.J. Teo, V.P. Bui, G. Yang, R. Martinez-Botas, Electromagnetic actuator design analysis using a two-stage optimization method with coarse–fine model output space mapping, IEEE Trans. Ind. Electron. 61 (10) (2014) 5453–5464, https://doi.org/10.1109/TIE.2014.2301727
[20] J. Song, G. Zhao, B. Li, J. Wang, Design optimization of PVDF-based piezoelectric energy harvesters, Heliyon 3 (9) (2017) 1–18, https://doi.org/10.1016/j.heliyon.2017.e00377
[21] Z. He, J. Lei, J. Yang, H. Zhu, Multi objective optimization and experimental investigation of the stirring performance of a novel micro actuator, Sci. Rep. 15 (1) (2025) 1–22, https://doi.org/10.1038/s41598-025-02701-9
[22] T. Janßen, A. Schütz, P.M. Weber, U. Wallrabe, T. Bechtold, Numerical design study of a multistable magnetic actuator, in: 26th International Conference on Thermal, Mechanical and Multi-Physics Simulation and Experiments in Microelectronics and Microsystems (EuroSimE), 2025, pp. 1–5, https://doi.org/10.1109/EuroSimE65125.2025.11006555
[23] Aaronia AG, MagnoShield flex Datasheet. Aaronia AG https://cdn-reichelt.de/documents/datenblatt/D100/AAR_MS_F_DB-EN.pdf (accessed 21 June 2026). Technical datasheet.
[24] A. Vučković, D. Vučković, M. Perić, B.M. Ranđelović, Quantitative analysis of magnetic force of axial symmetry permanent magnet structure using hybrid boundary element method, Symmetry 16 (11) (2024), https://doi.org/10.3390/sym16111495
[25] J.M. Camacho, V. Sosa, Alternative method to calculate the magnetic field of permanent magnets with azimuthal symmetry, Rev. Mex. Física E 59 (1) (2013) 8–17.

[26] W. Robertson, B. Cazzolato, A. Zander, A simplified force equation for coaxial cylindrical magnets and thin coils, IEEE Trans. Magn. 47 (8) (2011) 2045–2049, https://doi.org/10.1109/TMAG.2011.2129524

[27] MATLAB Global Optimization Toolbox, MATLAB Global Optimization Toolbox, The MathWorks, Natick, MA, USA, 2022.

[28] J. Zhang, Y.C. Lee, V.M. Bright, J. Neff, Digitally positioned micromirror for open-loop controlled applications, pp. 536–539, 2002, https://doi.org/10.1109/MEMSYS.2002.984327

[29] S.R. Samuelson, H. Xie, A large piston displacement MEMS mirror with electrothermal ladder actuator arrays for ultra-low tilt applications, J. Microelectromechanical Syst. 23 (1) (2013) 39–49, https://doi.org/10.1109/JMEMS.2013.2290994

[30] T. Schiepp, R. Schnetzler, L. Riccardi, M. Laufenberg, Energy-efficient multistable valve driven by magnetic shape memory alloys, in: 10th International Fluid Power Conference (IFK), vol. 3, 2016, pp. 491–502.

[31] A. Mohand-Ousaid, I. Bouhadda, G. Bourbon, P. Le Moal, Y. Haddab, P. Lutz, Compact digital microrobot based on multistable modules, IEEE Robot. Autom. Lett. 6 (2) (2021) 1926–1933, https://doi.org/10.1109/LRA.2021.3061003

[32] B. Wang, J. Shen, C. Huang, Z. Ye, J. He, X. Wu, Z. Guo, L. Zhang, T. Xu, Magnetically driven biohybrid blood hydrogel fibres for personalized intracranial tumour therapy under fluoroscopic tracking, Nat. Biomed. Eng. 9 (9) (2025) 1471–1485, https://doi.org/10.1038/s41551-025-01382-z

[33] C. Huang, Z. Lai, X. Wu, T. Xu, Multimodal locomotion and cargo transportation of magnetically actuated quadruped soft microrobots, Cyborg Bionic Syst. (2022), https://doi.org/10.34133/cbsystems.0

Author biography

Pascal Manuel Weber completed his B.Sc. (2018) and M.Sc. (2022) in Embedded Systems Engineering at the University of Freiburg, Germany. He is currently a Ph.D. student in the Laboratory of Microactuators at IMTEK Freiburg. His interests lie in mechanical and electrical engineering, as well as embedded programming for microprocessors.

Michael Olbrich received his B.Sc. and M.Sc. degrees in electrical engineering from the Technical University of Munich in 2017 and 2019, respectively. He is currently a Research Assistant with the Department of Computer Science, Chair of Control Engineering at the University of Augsburg, where he is pursuing his Ph.D. degree. His research interests include optimal trajectory planning and control, particularly in applications to microactuators.

Yannik Tim Rüde completed his B.Sc. (2024) in Microsystems Engineering at the University of Freiburg, Germany. He is currently enrolled as a master's student in Microsystems Engineering and works as a research assistant in the Laboratory of Microactuators at IMTEK Freiburg. His research interests lie in mechanical engineering and materials science.

Christoph Ament has been a professor of control engineering at the University of Augsburg, Germany since 2015. He studied electrical engineering in Karlsruhe, received his PhD from Ulm University and was a professor at the universities of Freiburg and Ilmenau. His research interests include precision control of microsystems and robots, data-based modeling and identification.

Ulrike Wallrabe studied physics at Karlsruhe University and completed her PhD on microturbines and micromotors in 1992 at University of Karlsruhe (today KIT). She then worked at the Institute for Microstructure Technology of Forschungszentrum Karlsruhe (today KIT) as a group leader for medical microsystems and micro optical devices. Since 2003, Ulrike Wallrabe has been a professor of microactuators at the Department of Microsystems Engineering - IMTEK- at University of Freiburg where her work focuses on magnetic microsystems, wireless power transfer, and adaptive micro optics actuated by piezoelectric actuators. In 2022 she won the Collaborative Research Center (SFB-1537) ECOSENSE together with Christiane Werner, also from the University of Freiburg.